

See discussions, stats, and author profiles for this publication at: <https://www.researchgate.net/publication/271382302>

High-efficiency photocatalytic activity of type II SnO/Sn₃O₄ heterostructures via interfacial charge transfer

ARTICLE *in* CRYSTENGCOMM · AUGUST 2014

Impact Factor: 4.03 · DOI: 10.1039/C4CE00884G

CITATIONS

4

READS

15

7 AUTHORS, INCLUDING:



Weiwei Xia

Yangzhou University

31 PUBLICATIONS 161 CITATIONS

SEE PROFILE



Xianghua Zeng

Yangzhou University

54 PUBLICATIONS 173 CITATIONS

SEE PROFILE



Jun Zhu

Yangzhou University

42 PUBLICATIONS 413 CITATIONS

SEE PROFILE



Min Zhou

Yangzhou University

18 PUBLICATIONS 115 CITATIONS

SEE PROFILE

High-efficiency photocatalytic activity of type II SnO/Sn₃O₄ heterostructures *via* interfacial charge transfer†

 Cite this: *CrystEngComm*, 2014, 16, 6841

 Received 26th April 2014,
Accepted 2nd June 2014

 Weiwei Xia,^{‡,*a} Haibo Wang,^{‡,a} Xianghua Zeng,^{*a} Jie Han,^b Jun Zhu,^a Min Zhou^a and Shudong Wu^a

DOI: 10.1039/c4ce00884g

www.rsc.org/crystengcomm

Flower-like hollow microspheres were synthesized on a large scale using a one-step hydrothermal route. The as-prepared products were characterized by X-ray diffraction (XRD), scanning electron microscopy (SEM), high-resolution transmission electron microscopy (HRTEM), X-ray photoelectron spectroscopy (XPS), and UV-vis diffuse reflectance spectroscopy. The results showed that the shells of the hollow microspheres were composed of numerous type II SnO/Sn₃O₄ heterostructures. A 500 °C annealing treatment changed the type II SnO/Sn₃O₄ heterostructures into type I SnO₂/Sn₃O₄ heterostructures; at 700 °C, the products were pure SnO₂ semiconductors. A photocatalytic degradation test showed that the highest efficiency degradation of rhodamine B (RhB) was obtained using type II SnO/Sn₃O₄ heterostructure semiconductors with a degradation rate constant of $2.3 \times 10^{-3} \text{ min}^{-1}$. This highly efficient activity was induced by enhanced charge separation in type II SnO/Sn₃O₄ heterostructure semiconductors.

I. Introduction

In recent years, univalent tin oxides, such as SnO₂ and SnO, have attracted considerable interest as research subjects because of their wide-ranging applications in lithium-ion batteries,^{1,2} sensitized solar cells,^{3,4} chemical and biological sensors^{5,6} and photocatalytic activity.^{7–10} In addition to univalent tin oxides, heterovalent tin oxides (*e.g.*, Sn₃O₄, Sn₂O₃, and Sn₅O₆) with a variety of coordination structures have been a popular subject in both theoretical calculations and experimental studies on regulating the Sn(II)/Sn(IV) ratio.^{11,12} Moreover, heterovalent tin structures have been reported to

influence the physical properties of tin oxides. Park *et al.* found that heterovalent tin oxide exhibits more sensitivity for CH₂Cl₂ detection than either SnO or SnO₂ univalent oxides.¹³ Theoretical calculations have confirmed that Sn₃O₄ has absorption bands that enable its use as a visible-light-driven photocatalyst for environmental remediation.¹⁴

A univalent tin oxide-based composite, which includes SnO₂ and SnO, is a wide band gap semiconductor (SnO₂: $\approx 3.5 \text{ eV}$, RT, SnO: $\approx 2.7 \text{ eV}$, RT) and exhibits good activity and stability under irradiation in both acidic and basic media. However, there have been few reports on the direct use of pure tin oxide-based materials as photocatalysts, and it is well-known that SnO₂ exhibits low photocatalytic activity even under UV irradiation because of its large band gap.^{15,16} Currently, there are primarily two popular strategies that have been pursued in the literature to improve the photocatalytic activity of SnO₂. One strategy is to design various geometries and morphologies for tin oxide-based photocatalysis, because catalytic activity depends on the structural parameters of SnO₂ such as geometry, morphology, *etc.*, and many complex nanostructures with novel geometry and morphology have been abundantly documented.¹⁷ Among the aforementioned nanostructures, hollow structures of tin oxide-based architectures have also been extensively investigated for their large catalytically active surface area, high organic pollutant adsorption and excellent incident light scattering within the structures.¹⁸ Although considerable progress has been made in the synthesis of hollow spheres,^{19,20} it is still a major challenge to develop a facile route for the preparation of tin oxide hollow nanostructures with the desired optical properties, especially a one-step synthesis of a hollow structure. However, this strategy does not fundamentally solve the problem of the fast recombination of photogenerated electron-hole pairs that hinder the industrial application of photocatalytic techniques. Thus, minimizing the recombination of photogenerated electron-hole pairs before they participate in redox processes is critical to the enhancement of photocatalytic

^a College of Physics Science and Technology & Institute of Optoelectronic Technology, Yangzhou University, Yangzhou 225002, PR China. E-mail: wxia@yzu.edu.cn, xhzeng@yzu.edu.cn

^b School of Chemistry and Chemical Engineering, Yangzhou University, Yangzhou 225002, PR China

† Electronic supplementary information (ESI) available. See DOI: 10.1039/c4ce00884g

‡ These authors contributed equally to this work.

efficiency. A novel development has been the synthesis of tin oxide-based photocatalysts using lower band gap semiconductors to form heterostructures (e.g., $\text{SnO}_2/\text{TiO}_2$,^{21,22} SnO_2/ZnO ,^{23,24} $\text{SnO}_2/\text{SnS}_2$,²⁵ SnO_2/Cd ,²⁶ and $\text{SnO}_2\text{--CdSe}$ ²⁷). Among these heterostructures, type II heterostructures are ideal for photocatalytic reactions in which both rapid charge separation and low radiative recombination efficiency are required. The improved photocatalytic activity of the hetero-junctions has also been attributed to a large extent to the enhanced separation of photo-induced electrons and holes *via* interfacial charge transfer. Photocatalytic activity can be enhanced by the type II heterostructures that are formed using two types of semiconductors; however, the fabrication of these structures is complex because two steps are usually required.

The close correlation between shape and morphology and the use of heterogeneous photocatalysts makes the facile fabrication of desirable hollow nanoarchitectures of tin oxide heterostructures a strongly desirable goal. Heterovalent tin oxides (e.g., Sn_3O_4 , Sn_2O_3 , and Sn_5O_6) exhibit a narrower band gap than that of univalent tin oxides^{28,29} and are thus candidates for producing heterostructures of type II univalent tin oxides. To the best of our knowledge, this study is the first to report on the photocatalytic activity of the heterostructures of a homologous series of tin oxides. Herein, we report a simple one-step hydrothermal route to fabricate $\text{SnO}/\text{Sn}_3\text{O}_4$ and $\text{SnO}_2/\text{Sn}_3\text{O}_4$ hetero-junctions for use as photocatalysts. Heterostructures of homologous tin oxides exhibit excellent photocatalytic performance. Notably, the annealing temperature can be simply tuned to easily control the band structure of tin oxides, thereby improving the optical properties of these materials. The heterostructures of tin oxides exhibit a much higher efficiency than pure SnO_2 for the degradation of rhodamine B (RhB). Moreover, this simple one-step hydrothermal route a wide range of practical applications and is a good strategy for employing heterovalent tin oxide to fabricate a homologous series of tin oxides for use as photocatalysts.

II. Experimental section

The aforementioned heterostructure microspheres with hollow structures were prepared by a facile one-step hydrothermal approach using sodium hydroxide, urea, and tin dichloride dehydrate ($\text{SnCl}_2 \cdot 2\text{H}_2\text{O}$) as precursors. In a typical synthesis, 60 ml of absolute ethanol and 140 ml of deionized water were mixed in a 250 ml beaker and stirred to ensure complete mixing. Then, 0.48 mM sodium hydroxide, 0.264 mM urea, and 0.04 mM tin dichloride dehydrate were dissolved in the mixture and agitated for approximately 1 h. The resulting mixture was transferred into a 200 ml sealed autoclave and heated in an oven at 180 °C for 18 h. The product was then centrifuged several times alternately in deionized water and ethanol, and the residue was dried for 10 h at 60 °C in a vacuum stove. The final product was then annealed at 300, 400, 500, 600 and 700 °C for 2 h under atmospheric conditions.

The morphologies of the obtained products were characterized using a field-emission scanning electron microscope

(FESEM, s-4800II, Hitachi, 15 kV). High-resolution transmission electron microscopy (HRTEM) images and selected area electron diffraction (SAED) patterns were captured using a Tecnanai G2 F30 S-Twin microscope at an accelerating voltage of 300 kV. Crystallographic data were obtained using power X-ray diffraction (Bruker, D8 Advance, Cu α radiation, $\lambda = 1.5406 \text{ \AA}$). The phase composition of the as-prepared product was analyzed using an Axis Ultra X-ray photoelectron spectroscope (XPS, Kratos Analytical Ltd., UK) equipped with a standard monochromatic Al- α source ($h\nu = 1486.6 \text{ eV}$). The binding energy data were calibrated with respect to the C1s signal of the ambient hydrocarbons (C-H and C-C) at 284.8 eV. The absorption measurements were performed using a UV-vis-NIR spectrophotometer (UV-vis, Cary-5000, Varian) with an integrating sphere.

Photocatalytic experiments were conducted on the as-prepared samples to decompose or remove rhodamine B (RhB) aqueous solutions using the following procedure: 5 mg of the as-prepared samples were suspended in 25 ml of an aqueous solution of $1 \times 10^{-5} \text{ mol L}^{-1}$ RhB. Prior to irradiation, the suspensions were sonicated for 10 min and then magnetically stirred in the dark for 30 min to attain desorption-adsorption equilibrium. The solution was then exposed to UV irradiation from a mercury lamp (300 W) at room temperature. Five-milliliter samples were collected every 30 min and centrifuged to remove the residual photocatalyst, and then the upper clear liquid was analyzed by recording the maximum absorption band (554 nm for RhB) using a Shimadzu UV-3600 spectrophotometer. Also, 5 mg of commercial TiO_2 (P25) was used in the control experiment. Additionally, the recycling experiments were performed for five consecutive cycles with an irradiation time of 150 min under UV irradiation to test the durability; the irradiation time was kept constant.

III. Results and discussion

The XRD patterns of the as-prepared samples and the tin oxide-based powders formed at varying oxidation temperatures of 300, 400, 500, 600, and 700 °C are shown in Fig. 1. The as-prepared tin oxide-based powders that were annealed at 300 and 400 °C exhibited two sharp diffraction peaks corresponding to the reflections of a tetragonal SnO phase (JCPDS 06-0395). A weak SnO peak was also observed at 29.989° (corresponding to the (101) plane), indicating the simultaneous existence of the tetragonal SnO phase. Note that extra peaks from minor phases could also be identified. The inset in Fig. 1(a) is an enlarged spectrum over the 22° to 35° range. In addition to the SnO peaks, six characteristic peaks could be identified (which are marked by (●)) as (101), ($\bar{1}20$), (111), ($\bar{2}10$), ($\bar{1}21$), and (210) reflections from Sn_3O_4 (JCPDS 16-0737). Following annealing above 400 °C, the XRD spectra of the samples changed dramatically. The peaks corresponding to SnO completely disappeared at 500 °C, and new dominant peaks that were attributed to the tetragonal SnO_2 phase (JCPDS 41-1445) appeared, indicating the oxidation of

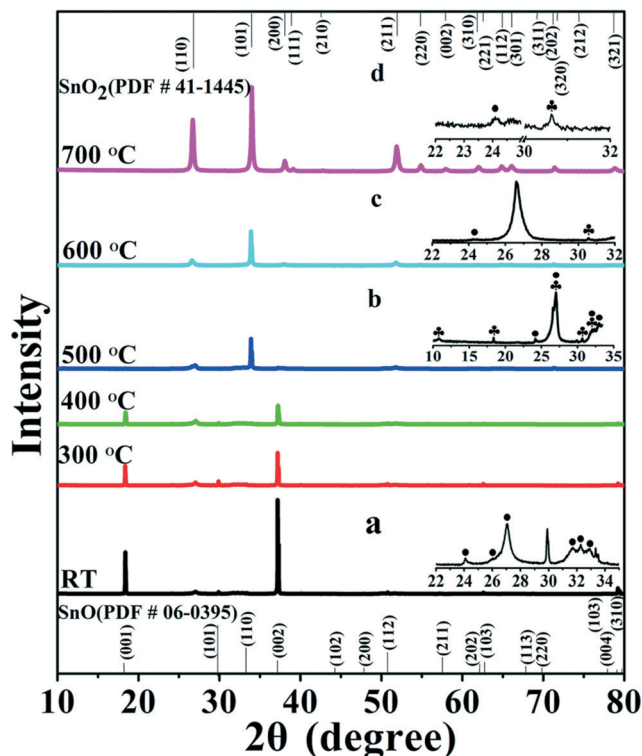


Fig. 1 XRD patterns of tin oxide-based powders before and after annealing at 300, 400, 500, 600, and 700 °C for 2 h in air; insets show expanded powder XRD patterns of samples before and after annealing at 500, 600, and 700 °C: inset (a) shows an enlarged spectrum, where peaks marked by (●) correspond to Sn_3O_4 (JCPDS 16-0737); inset (b) shows an enlarged spectrum, where peaks marked by (♣) correspond to other Sn_3O_4 phases (JCPDS 20-1293).

SnO to SnO_2 . The phase transformation process is discussed later (see experimental details in ESI†, S1). Furthermore, the intensities of the SnO_2 diffraction peaks increased with the annealing temperature. At 500 and 600 °C, two typical Sn_3O_4 peaks were simultaneously present. The inset in Fig. 1(b) shows that the peaks marked by (♣) were attributed to the (001), (100), (101), (111), (020), (021), and ($\bar{1}$ 12) reflections of Sn_3O_4 (JCPDS 20-1293). When the annealing temperature reached 700 °C, the products were transformed into pure rutile-structured SnO_2 , which was confirmed by fitting the SnO_2 peaks (JCPDS 41-445), as shown in the inset of Fig. 1(d). Therefore, a phase transition from SnO to SnO_2 occurred along with the formation of an intermediate oxidation state of Sn_3O_4 . The existence of Sn_3O_4 was confirmed by Raman spectroscopy to clarify the crystalline compositions and structures of the aforementioned samples (see experimental details in ESI†, S2).

To gain insight into the evolution of the tin oxide during the annealing process, X-ray photoelectron spectroscopy (XPS) was performed to investigate the changes in the Sn-related states under different annealing temperatures (see Fig. 2). The Sn 3d spectrum exhibited spin-orbit doublet peaks at ≈ 486 eV ($\text{Sn}^{2+} 3d_{5/2}$) and ≈ 495 eV ($\text{Sn}^{2+} 3d_{3/2}$). After annealing above 500 °C, the main peaks shifted to higher binding energies, which matched the binding energies of Sn^{4+} (at 486.7 eV

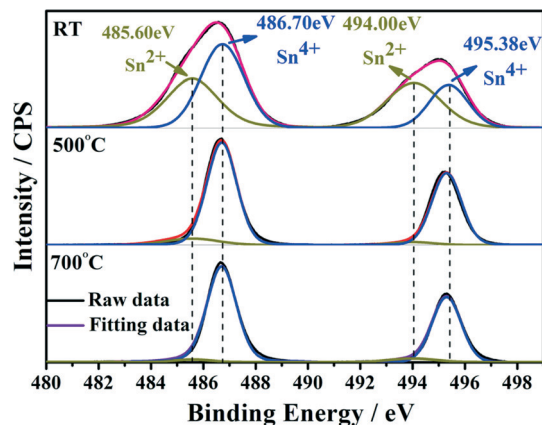


Fig. 2 XPS spectra of Sn 3d for tin oxide-based powders before and after annealing at 500 and 700 °C for 2 h in air.

and 495.4 eV for $3d_{5/2}$ and $3d_{3/2}$, respectively) well, and the Sn^{4+} content increased and gradually dominated the material composition. The binding energies of the Sn-related states obtained in this experiment were consistent with the XRD results.

The product morphologies were studied by SEM. Fig. 3 shows typical SEM images of the collected tin oxide microspheres before and after annealing treatments at different temperatures. Three-dimensional (3D) microspheres assembled into sheet-like subunits with diameters ranging from 3 to 5 μm . TEM measurements were performed to characterize the sample structures further and are shown in the inset in Fig. 3(a). The obvious contrast between the dark edges and the pale centers confirms that these microspheres were hollow. It has been reported that this hollow structure can improve light harvesting through multiple light reflections and scattering effects that can be used for applications in the photo-decomposition of organic compounds. Furthermore, the morphology of the hollow microsphere structures was faithfully preserved during the calcination process.

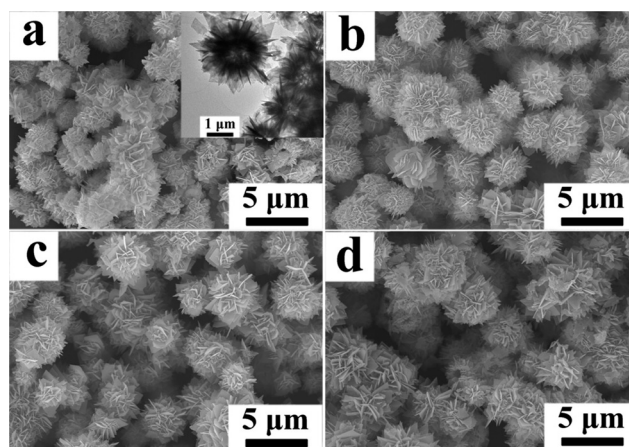


Fig. 3 SEM images of tin oxide-based microspheres (a) before and after annealing at (b) 300, (c) 500, and (d) 700 °C for 2 h in air; inset in (a) is a TEM image of the as-synthesized tin oxide microspheres.

Therefore, hollow microspheres can be synthesized on a large scale, where the shells of the microspheres are covered with numerous nanoflakes.

To obtain detailed information about the microstructure of the as-synthesized tin oxide-based microspheres, HRTEM and selected area electron diffraction (SAED) analyses were carried out: the results are shown in Fig. 4. The SAED patterns in the insets in Fig. 4 show two different types of crystal phases in the samples: both phases of the heterostructures were crystalline. Meanwhile, the HRTEM images of the region that are marked by a white line confirmed the presence of crystalline SnO/Sn₃O₄ and SnO₂/Sn₃O₄ crystal lattices in the interfacial region, as shown in Fig. 4(b, d). The HRTEM images also clearly reveal the *in situ* formation of heterostructures within the interface, which would have facilitated interfacial electron transfer and accordingly increased the photocatalytic activity. The aforementioned analysis confirmed that SnO/Sn₃O₄ and SnO₂/Sn₃O₄ composites with heterostructures formed in our prepared samples. Note that the SnO content in the SnO/Sn₃O₄ semiconductors disappeared as the annealing temperature increased, until finally, only SnO₂ was observed at 700 °C; thus, the annealing temperature could be tuned to adjust the tin oxide constituents to produce the required optical properties.

Typical UV-vis spectroscopy measurements were used to further confirm the formation of the heterostructures. In the literature,^{30,31} SnO₂ has been reported to be a direct band gap material, and SnO and Sn₃O₄ have been reported to be indirect band gap materials: the optical band gap energy (E_g) of these materials can be calculated using the equation given below:³²

$$\alpha h\nu = C(h\nu - E_g)^n$$

where n is equal to 1/2 and 2 for direct allowed transitions and indirect transitions, respectively.

The spectra of the SnO/Sn₃O₄ and SnO₂/Sn₃O₄ heterostructures are plotted in Fig. 5(a and c): two slopes that indicate the formation of heterostructures can be clearly observed. The E_g values of SnO and Sn₃O₄ in the SnO/Sn₃O₄ heterostructures were evaluated as 2.47 and 2.19 eV, respectively. Upon heating to 500 °C, the E_g values for SnO₂ and Sn₃O₄ in the SnO₂/Sn₃O₄ heterostructures were evaluated as 3.41 and 2.19 eV, respectively. Meanwhile, further increasing the annealing temperature to 700 °C yielded only one slope in Fig. 5(e), and the E_g was estimated at 3.61 eV, which was in agreement with the reported value for SnO₂ (3.5–3.7 eV). The valence band edge positions of the tin oxide-based

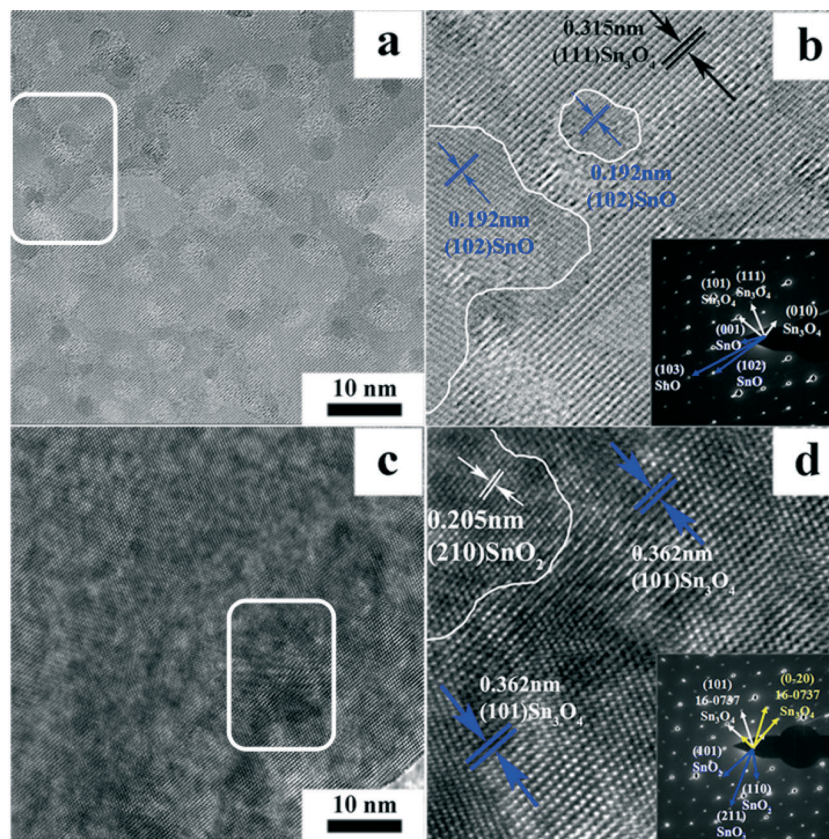


Fig. 4 Low-magnification TEM images of tin oxide-based heterostructures obtained (a) before and (c) after annealing at 500 °C for 2 h in air. (b, d) HRTEM images taken from (a) and (c), respectively. Insets of (b) and (d) show the corresponding SAED patterns.

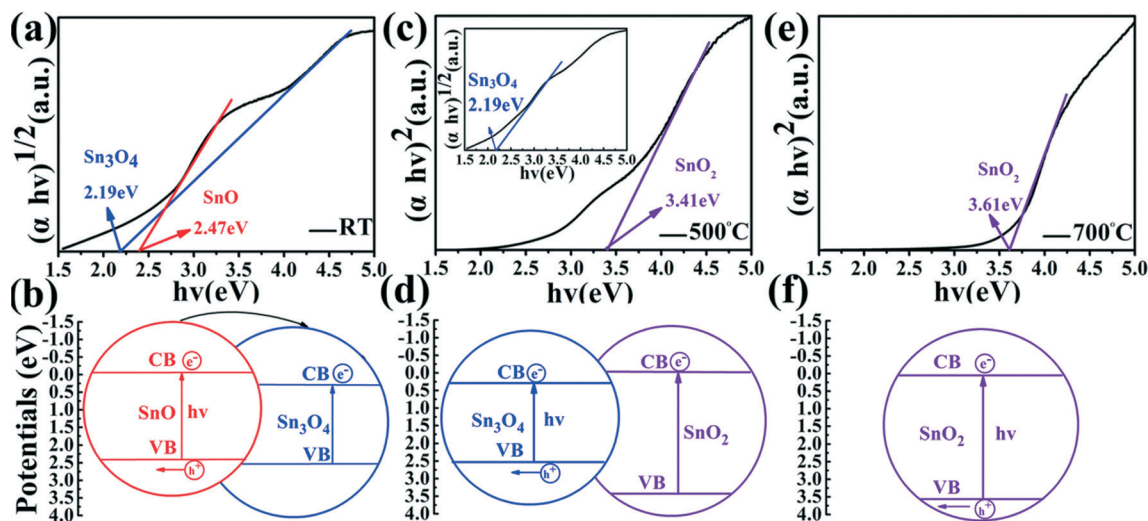


Fig. 5 Plots of $(\alpha hv)^{1/2}$ vs. photon energy ($h\nu$) for (a) as-prepared tin oxide-based heterostructures and heterostructures formed at oxidation temperatures of (c) 500 and (e) 700 °C; (b), (d) and (f) are the corresponding schematic diagrams of the energy band structures of tin oxide-based heterostructures.

heterostructures were estimated using electronegativity concepts. The valence band potentials of a semiconductor at the point of zero charge can be calculated using the following empirical equation:^{33–35}

$$E_{\text{VB}} = X - E^{\circ} + 0.5E_{\text{g}}, \quad (1)$$

where E_{VB} is the VB edge potential and X is the electronegativity of the semiconductor, which is the geometric mean of the electronegativity of the constituent atoms. The X values for SnO , SnO_2 and Sn_3O_4 are 5.68, 6.24 and 5.91 eV, respectively. The energy of the free electrons on the hydrogen scale is denoted by E° (≈ 4.5 eV), E_{g} is the band gap energy of the semiconductor, and E_{CB} can be determined from $E_{\text{CB}} = E_{\text{VB}} - E_{\text{g}}$. Fig. 5(b, d, and f) show the schematic diagrams of the energy band structures of the tin oxide-based heterostructures. Sn_3O_4 exhibited a narrower band gap than the band energy alignment of SnO and SnO_2 , and the valence and conduction band alignments for Sn_3O_4 were staggered relative to those of SnO and SnO_2 ; therefore $\text{SnO}/\text{Sn}_3\text{O}_4$ was a type II heterostructure.

In $\text{SnO}_2/\text{Sn}_3\text{O}_4$, the band gap of Sn_3O_4 was embedded in that of SnO_2 ; thus, $\text{SnO}_2/\text{Sn}_3\text{O}_4$ was a type I heterostructure.

The photocatalytic activities of the different as-synthesized heterostructures were evaluated by the degradation of RhB dye in water under UV light irradiation, as shown in Fig. 6(a). Fig. 6(a) shows the absorption spectra of the RhB solution in the presence of tin oxide-based semiconductors. Fig. 6(a) also clearly reveals that the tin oxide-based heterostructures $\text{SnO}/\text{Sn}_3\text{O}_4$ and $\text{SnO}_2/\text{Sn}_3\text{O}_4$ exhibited a better catalytic degradation than SnO_2 , whereas the $\text{SnO}/\text{Sn}_3\text{O}_4$ heterostructure semiconductors performed the most efficient degradation of RhB. The poor performance of SnO_2 semiconductors could be attributed to the low negative conduction potential of SnO_2 , because the conduction band bottom potential of SnO_2 is close to that of $\text{O}_2/\text{O}_2^{\cdot -}$ (-0.046 eV vs. SHE), indicating that SnO_2 readily undergoes photocorrosion in aqueous media containing oxygen and that the overpotential is too small to reduce O_2 with photoexcited electrons;³⁶ therefore, photocatalytic degradation using SnO_2 was not effective. For practical photocatalytic applications, the

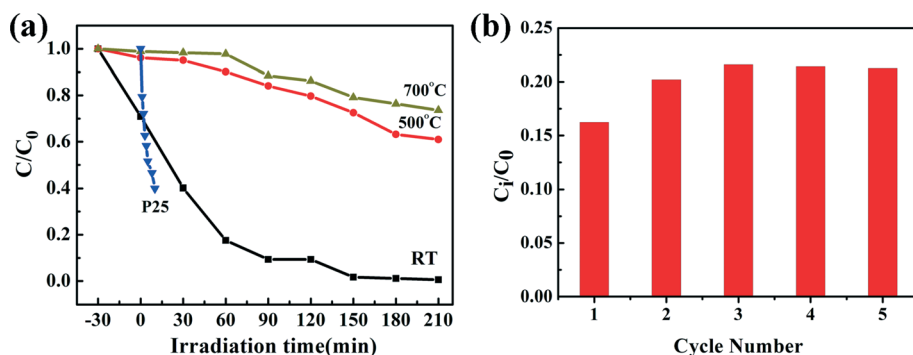


Fig. 6 (a) Comparison of photocatalytic degradation of RhB in the presence of tin oxide-based heterostructures; (b) cycling runs for the photocatalytic degradation of RhB over $\text{SnO}/\text{Sn}_3\text{O}_4$ under UV irradiation.

recycling of the photocatalyst is very important. In the durability tests, SnO/Sn₃O₄ was repeatedly used for the RhB photodegradation reaction 5 times (Fig. 6(b)). The experimental results indicated that no apparent deactivation of photocatalyst is seen after 5 cycles as compared to the fresh catalyst.

Catalytic degradations of dye have been reported in the literature.^{37,38} For SnO/Sn₃O₄ with a type II heterostructure, electrons could be excited from the valence bands to the conduction bands of SnO semiconductors by UV irradiation because of the band offset: the electrons generated on the conduction band of SnO were directly injected into the conduction band of Sn₃O₄, whereas the holes remained on the valence band (as shown in Fig. 5(b)). Thus, more electrons accumulated in the conduction band of the SnO, resulting in more holes in the valence band of SnO, *i.e.*, interfacial charge separation occurred. The electrons that were eventually localized in the conduction band of Sn₃O₄ reduced O₂ to form superoxide ions *O₂⁻, and the holes located in the valence band of SnO reacted with the hydroxyl group to produce the hydroxyl radicals (*OH) that degraded RhB in the photoreaction. The highly-efficient photodegradation activity of SnO/Sn₃O₄ can be explained as follows: on the one hand, as the morphology of SnO/Sn₃O₄ exhibits a high surface-to-volume ratio, which is beneficial to the adsorption of dye RhB molecules, the photodegradation efficiency improves; on the other hand, the life span of the photogenerated electron-hole pair is long enough for it to migrate and be available for redox reactions at the photocatalyst surface; the recombination rate of the electron and hole excited from the indirect semiconductor SnO is lower than that of the direct semiconductor, which is favorable for the charge separation. Therefore, the SnO/Sn₃O₄ samples prepared at room temperature show a highly efficient photodegradation activity, as shown in Fig. 6.

For the type I SnO₂/Sn₃O₄ heterostructure, electrons were excited upon light irradiation of both the SnO₂ and the Sn₃O₄ semiconductors. Then, unlike in the type II heterostructures, more electrons and holes recombined while electrons and holes were produced for both the SnO₂ and Sn₃O₄ semiconductors, resulting in a photocorrosion effect as the electrons and holes recombined in the conduction and valence bands of SnO₂ and Sn₃O₄. Sn₃O₄ is an indirect semiconductor; therefore, the recombination rate of the indirect semiconductor is relatively low, and some electrons and holes participated in the photocatalytic degradation of RhB before recombination, which explains why the type I SnO₂/Sn₃O₄ heterostructure had a much higher photocatalytic degradation effect than the SnO₂ semiconductor. The degradation efficiency of a photocatalyst can be defined as follows:³⁹

$$\text{Degradation}(\%) = (1 - C/C_0) \times 100\%, \quad (2)$$

where C_0 is the RhB concentration at equilibrium adsorption and C is the residual concentration of RhB at different illumination intervals. The photodegradation of RhB

follows pseudo-first-order kinetics, which can be expressed as follows:

$$\ln(C/C_0) = -kt, \quad (3)$$

where k (min⁻¹) is the degradation rate constant. Eqn (3) was used to calculate the degradation rate constants of 2.3×10^{-3} and 3.6×10^{-5} min⁻¹ for the SnO/Sn₃O₄ and SnO₂/Sn₃O₄ semiconductors, respectively. However, the degradation rate constant for SnO/Sn₃O₄ is much smaller than that of P25 (9.2×10^{-2}). We believe that our report provides a new approach to realize the highly efficient photocatalytic activity of heterostructures of type II univalent tin oxides. Therefore, enhanced photocatalytic degradation of RhB solutions was observed using SnO/Sn₃O₄ with type II heterostructures as photocatalysts, as shown in Fig. 6. The observed phenomenon was consistent with other reports.⁴⁰ Furthermore, the flower-like hollow microspheres still remained after five consecutive cycles (see Fig. S3 in the ESI†).

IV. Conclusions

In summary, tin oxide semiconductors with a morphology of flower-like hollow microspheres were synthesized using a one-step hydrothermal route and a series of annealing processes. The as-prepared products were characterized by XRD, scanning electron microscopy (SEM), high-resolution transmission electron microscopy (HRTEM), X-ray photoelectron spectroscopy (XPS), and UV-vis diffuse reflectance spectra. Systematic measurements revealed that the as-prepared flower-like hollow microspheres had a type II SnO/Sn₃O₄ heterostructure. After a 500 °C annealing treatment, the original SnO/Sn₃O₄ heterostructure changed into SnO₂/Sn₃O₄ with a type I heterostructure, and the product was SnO₂ at 700 °C. The prepared original SnO/Sn₃O₄ semiconductors with type II heterostructures performed the highest efficiency degradation of rhodamine B (RhB) with a degradation rate constant of 2.3×10^{-3} min⁻¹. This highly efficient activity was induced by the enhanced charge separation in the SnO/Sn₃O₄ semiconductors with type II heterostructures. This typical hollow structure has two advantages for photocatalytic activity: the structure has a high surface-to-volume ratio, which enables multi-reflections of irradiated light within the interior cavities, and the products consist of two phases of homologous tin oxides. We believe that our prepared SnO/Sn₃O₄ and SnO₂/Sn₃O₄ heterostructure microspheres can be used as visible-light-driven high-performance photocatalysts. Studies on such applications are currently under way.

Acknowledgements

We gratefully acknowledge the financial support from Yangzhou Science and Technology Development (no. YZ2011150), the Natural Science Foundation of Education Bureau of Jiangsu Province, China (grant no. 12KJB140012), the National Natural Science Foundation of China (no. 21273004) and the Priority

Academic Program Development of Jiangsu Higher Education Institutions. We would also like to acknowledge the technical support from the Testing Center of Yangzhou University.

References

- 1 P. Meduri, C. Pendyala, V. Kumar, G. U. Sumanasekera and M. K. Sunkara, *Nano Lett.*, 2009, **9**(2), 612.
- 2 Z. Y. Wang, D. Y. Luan and X. W. Lou, *J. Am. Chem. Soc.*, 2011, **133**(13), 4738.
- 3 H. J. Snaith and C. Ducati, *Nano Lett.*, 2010, **10**(4), 1259.
- 4 M. A. Hossain, G. W. Yang, M. Parameswaran, J. R. Jennings and Q. J. Wang, *J. Phys. Chem. C*, 2010, **114**(49), 21878.
- 5 J. T. McCue and J. Y. Ying, *Chem. Mater.*, 2007, **19**(5), 1009.
- 6 J. Huang, N. Matsunaga, J. Shimanoe, N. Yamazoe and T. Kunitake, *Chem. Mater.*, 2005, **17**(13), 3513.
- 7 L. R. Zheng, Y. H. Zheng, C. Q. Chen and J. F. Zhu, *Inorg. Chem.*, 2009, **48**(5), 1819.
- 8 Y. C. Zhang, Z. N. Du and D. D. Dionysiou, *ACS Appl. Mater. Interfaces*, 2011, **3**(5), 1528.
- 9 C. M. Fan, Y. Peng, Q. Zhu and A. W. Xu, *J. Phys. Chem. C*, 2013, **117**(46), 24157.
- 10 A. K. Sinha, P. K. Manna and M. Pradhan, *Chem. Commun.*, 2014, **50**, 2847.
- 11 A. Seko, A. Togo and I. Tanaka, *Phys. Rev. Lett.*, 2008, **100**, 45702.
- 12 M. S. Moreno, R. F. Egerton and P. A. Midgley, *Phys. Rev. B: Condens. Matter Mater. Phys.*, 2004, **69**, 041307.
- 13 S. H. Park, Y. C. Son, W. S. Willis, S. L. Suib and K. E. Creasy, *Chem. Mater.*, 1998, **10**(9), 2389.
- 14 O. M. Berengue, R. A. Simon and A. J. Chiquito, *J. Appl. Phys.*, 2010, **107**, 033717.
- 15 H. J. Wang, F. Q. Sun and Y. Zhang, *J. Mater. Chem.*, 2010, **20**, 5641.
- 16 C. Nasr, P. V. Kamat and S. Hotchandani, *J. Electroanal. Chem.*, 1997, **420**, 201.
- 17 S. W. Liu, G. C. Huang, J. G. Yu and P. K. Wong, *ACS Appl. Mater. Interfaces*, 2014, **6**(4), 2407.
- 18 H. J. You, R. Liu, C. C. Liang and B. J. Ding, *J. Mater. Chem. A*, 2013, **1**, 4097.
- 19 L. Xu, M. P. Steinmiller and S. E. Skrabalak, *J. Phys. Chem. C*, 2012, **116**(24), 871.
- 20 M. T. Niu, F. Huang, L. F. Cui and Y. S. Wang, *ACS Nano*, 2010, **4**(2), 681.
- 21 K. Vinodgopal, I. Bedja and P. V. Kamat, *Chem. Mater.*, 1996, **8**(8), 2180.
- 22 Z. Y. Liu, D. D. Sun, P. Guo and J. O. Leckie, *Nano Lett.*, 2007, **7**(4), 1081.
- 23 M. T. Uddin, Y. Nicolas, C. Olivier, T. Toupance, L. Servant, M. M. Muller, H. J. Kleebe, J. Ziegler and W. Jaegermann, *Inorg. Chem.*, 2012, **51**(14), 7764.
- 24 J. S. Lee, O. S. Kwon and J. Jang, *J. Mater. Chem.*, 2012, **22**, 14565.
- 25 Y. C. Zhang, Z. N. Du, K. W. Li, M. Zhang and D. D. Dionysiou, *ACS Appl. Mater. Interfaces*, 2011, **3**, 1528.
- 26 A. Kar, S. Kundu and A. Patra, *RSC Adv.*, 2012, **2**, 10222.
- 27 C. Nasr, P. V. Kamat and S. Hotchandani, *J. Electroanal. Chem.*, 1997, **420**, 201.
- 28 F. P. Wang, X. T. Zhou, J. G. Zhou and T. K. Sham, *J. Phys. Chem. C*, 2007, **111**(51), 18839.
- 29 Y. H. He, D. Z. Li, J. Chen, Y. Shao and J. J. Xian, *RSC Adv.*, 2014, **4**, 1266.
- 30 M. Losurdo, D. Barreca, P. Capezzuto, G. Bruno and E. Tondello, *Surf. Coat. Technol.*, 2002, **151**, 2.
- 31 F. Demichelis, V. Smurro, A. Tagliaferro and E. Tresso, *J. Phys. D: Appl. Phys.*, 1985, **18**, 1825.
- 32 H. Deng and J. M. Hossenlopp, *J. Phys. Chem. B*, 2005, **109**(1), 66.
- 33 M. A. Butler and D. S. Ginley, *J. Electrochem. Soc.*, 1978, **125**(2), 228.
- 34 X. Lin, J. Xing, W. Wang, Z. Shan, F. Xu and F. Huang, *J. Phys. Chem. C*, 2007, **111**(49), 18288.
- 35 X. Zhang, L. Zhang, T. Xie and D. Wang, *J. Phys. Chem. C*, 2009, **113**(17), 7371.
- 36 X. Xu, R. Lu, X. Zhao, S. Xu, X. Lei, F. Zhang and D. G. Evans, *Appl. Catal., B*, 2011, **102**, 147.
- 37 R. M. Navarro, F. D. Valle and J. A. V. de la Mano, *Adv. Chem. Eng.*, 2009, **36**, 111.
- 38 H. H. Mohamed and D. W. Bahnemann, *Appl. Catal., B*, 2012, **128**, 91.
- 39 V. Taghvaei, A. Habibi-Yangjeh and M. Behboudnia, *Phys. E*, 2010, **42**(7), 1973.
- 40 X. M. Xiang, L. J. Chou and X. H. Li, *Phys. Chem. Chem. Phys.*, 2013, **15**, 19545.